Colloidal Quantum Dots Intraband Photodetectors

Zhiyou Deng, Kwang Seob Jeong, and Philippe Guyot-Sionnest*

James Franck Institute, 929 East 57th Street, Chicago, Illinois 60637, United States

ABSTRACT Photoconductivity is demonstrated with monodispersed HgSe colloidal quantum dots that are illuminated with radiation resonant with $1S_e-1P_e$ intraband electronic absorption, between 3 and 5 μm. A doping of two electrons per dot gives the lowest dark current, and a detectivity of 8.5×10^8 Jones is obtained at 80 K. Photoluminescence of the intraband transition is also observed. The detector properties are discussed in terms of the measured photoluminescence quantum yield, the electron mobility in the $1P_e$ state, and the responsivity. The intraband photoresponse allows to fully harness the quantum confined states in colloidal nanostructures, extending the prior limited use of interband transition.

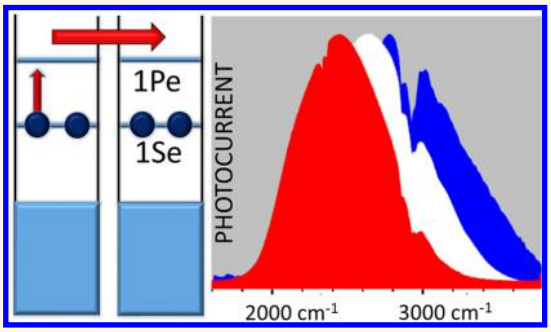

KEYWORDS: mercury selenide · colloidal quantum dots · intraband photoconductivity · intraband absorption · infrared photodetector

For the past three decades colloidal quantum dots (CQD) have been exclusively used for their interband transitions.[1] In contrast, intraband or intersubband transitions have been used with great success in epitaxially grown nanostructures.[2] Indeed, a whole new perspective was possible when quantum wells of wide band gap semiconductor were shown to exhibit intense infrared transitions that could be controlled by the thickness.[3] Quantum well infrared detectors (QWIP) based on the wide gaps GaAs/AlGaAs were among the first devices to use these intersubband transitions,[4] and QWIPs are now a commercial alternative to the traditional Mercury–Cadmium–Telluride (MCT) detectors. Of even greater impact, the quantum cascade lasers (QCL), first demonstrated two decades ago,[5] used precise engineering of the intersubband energies and relaxation rates. This major achievement has spurred tremendous activity in semiconductor physics and device development, and QCLs are now the most widely used mid-IR tunable laser source. In principle, the use of intraband transition in CQDs should also lead to many novel opportunities, but there are several challenges. Early on, the ultrafast excitonic relaxation of CQDs[6,7] seemed to preclude any application of higher excitonic states, although there are now reports of multiexcitons production in photovoltaic devices.[8,9] CQDs have ligands and surface states, and this can affect the intraband states and their relaxation.[10] Importantly, doping is difficult with CQDs,[11−13] while intraband application requires precise doping.

In this report, we introduce the first application of the intraband transition of doped quantum dots by demonstrating photoconductivity in the mid-infrared using the $1S_e-1P_e$ transition of doped HgSe quantum dots. Epitaxially grown quantum dots have promised higher temperature operation of infrared detectors[14,15] due to the long carrier lifetime associated with their discrete density of states.[16] However, the epitaxial quantum dots have suffered from low packing density and high fabrication cost. Colloidal quantum dot (CQD) IR detectors showed promise as very low cost materials with high packing density,[17−19] but mid-IR interband CQD detectors are restricted to semimetal or very small gap ternary alloys, and therefore, intraband CQD detectors can, in principle, allow many more materials for infrared applications.

For photoconduction using the intraband transition between the first two conduction band states $1S_e$ and $1P_e$ of an ideal spherical quantum dot, the dots must be doped with two electrons as shown in the schematic in Figure 1A. With a partially empty $1S_e$ state,

* Address correspondence to pgs@uchicago.edu.

Received for review September 9, 2014 and accepted October 24, 2014.

Published online October 24, 2014
10.1021/nn505092a

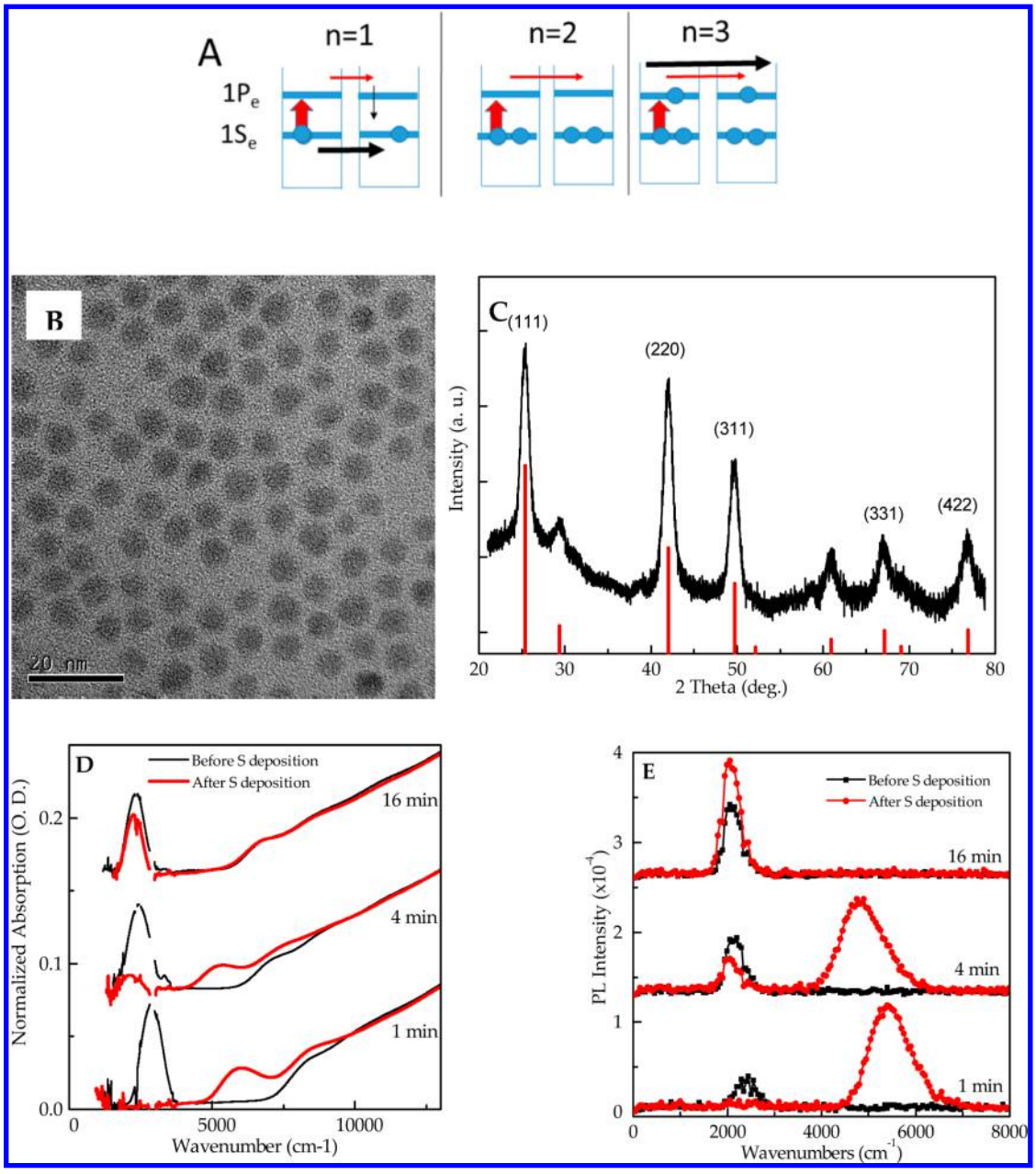

Figure 1. (A) Doping requirement for intraband conduction. The red horizontal arrow represents the photocurrent, and the black arrow is the dark current. A doping level of $n = 2$ minimizes the dark current. (B) TEM image of HgSe CQDs. The average diameter of the particles are 6.2 nm with a standard deviation of 0.76 nm. (C) The XRD data shows the peaks corresponding to zinc blende HgSe. (D) Absorption spectra of three samples of different reaction times in TCE, before and after sulfide deposition. The intraband absorptions are around 2500 cm^{-1}, red shifting with longer growth time. The sizes are in order of increasing growth time, 5.5, 5.9, and 6.2 nm with a standard deviation of ~0.7 nm (Supporting Information). (E) Photoluminescence of the samples, before and after sulfide deposition. The interband emission is around 5000 cm^{-1}.

the large dark current through the $1S_e$ states and rapid recombination of the electron in the $1P_e$ states with hole in the $1S_e$ states will prevent any measurable photoconduction. With $1S_e$ full and $1P_e$ partially filled, the large dark current through the $1P_e$ states will also overwhelm the photocurrent. $n = 2$, where n is the doping level per dot, is the best condition, as the dark current is minimized[14] and excited electrons in $1P_e$ have a lifetime limited by recombination with the photogenerated "holes" in the $1S_e$ states. In spite of this requirement, weak intraband photoconduction with CQDs has been reported using undoped CdSe nanocrystals dispersed in a conducting organic polymer,[20] but the result has not been confirmed.

RESULTS AND DISCUSSION

HgSe Quantum Dots Synthesis and Characterization. HgSe is a bulk semimetal that has been synthesized before as nanocrystals[21] with very small quantum dots showing clear excitonic absorption well into the visible.[22] The synthesis developed here is optimized for larger HgSe CQDs of about 5−7 nm diameter, which exhibit

intraband absorption in the 3−5 μm range. We use mercury(II) chloride, selenourea and oleylamine (OAm). During the reaction, the samples are extracted and growth is quenched using dodecanethiol ligands. The samples are then precipitated by addition of a polar solvent, such as methanol, and stored in tetrachloroethylene (TCE) or hexane/octane solutions for future use. The particles are spherical with a narrow size dispersion, as shown by the TEM in Figure 1B. TEM image analysis indicates a slow growth with average diameters of 5.5, 5.9 and 6.2 nm, with reaction time after injection of 1, 4, and 16 min, respectively. The XRD in Figure 1C shows that they have the bulk zinc blende crystal structure.

The absorption spectra of HgSe CQDs during the course of the reaction are shown in Figure 1D. As prepared, they show the intraband absorption peak around 2000−3000 cm^{-1} indicating stable doping, as well as interband absorption at higher energy. A two-band k.p model gives an intraband energy of 2500 cm^{-1}, and an interband energy of 5000 cm^{-1} for 6 nm diameter HgSe quantum dot (Supporting Information), which is in good agreement with the spectra and size in Figure 1D.

The relative intensities of the intraband and interband absorption vary with different reaction time, indicating different doping levels. It has recently become appreciated that the surface composition and the ligands of the CQDs allow to tune the absolute energy of the levels and the doping in a given environment.[23−25] The adsorption of sulfide ions,[26] which was previously shown to change the doping level in HgS CQDs,[24] affects the doping of the HgSe CQDs to varying degrees as shown in Figure 1D. The "1 min" sample starts out with a partially filled $1S_e$ as seen by the small interband absorption at ~5000 cm^{-1} therefore $n < 2$. For the small-sized dots from short reaction time, the sulfides quench fully the intraband absorption, $n = 0$, and the first interband excitonic peak appears. The well-resolved exciton peak reflects the good size control of the HgSe samples. The "4 min" sample shows no interband absorption around 5000 cm^{-1} so that the $1S_e$ state is full, but it can only be partially undoped by sulfides as seen by the remaining intraband absorption. The "16 min" sample also has a filled $1S_e$ state, but the sulfide has a weaker effect on the intraband and interband absorption suggesting $n > 2$. This shows that the synthesis produces dodecanethiol-capped HgSe CQDs with a range of doping around $n \sim 2$. The reproducibility of the synthesis is excellent, and the doping level of sample solutions is stable for weeks in ambient conditions. The systematic investigation of the effects of surface composition and size on the doping level will be a future direction to precisely control the doping.

Figure 1E shows the photoluminescence (PL) of the HgSe samples. The intraband PL is observed around 2500 cm^{-1} in accord with the absorption in Figure 1D. The observation of the intraband PL is significant since it indicates that the $1P_e$ lifetime is not so short. As mentioned earlier, a sub-ps $1P_e$ state lifetime had been obtained in early measurements in CdSe CQDs.[6,27] The ultrafast relaxation was attributed to an electron−hole Auger relaxation.[28] Later experiments achieved intraband lifetimes as long as 1 ns by removing the hole and reducing the spectral and spatial overlap with ligand vibrations.[29] Using an integrating sphere, the quantum yield is $QY = 1-5 \times 10^{-4}$ over a range of samples. With an estimated $1S_e-1P_e$ radiative lifetime of $\tau_r \sim 0.6\ \mu s$ in TCE (Supporting Information), the $1P_e$ lifetime, $\tau_1 = \tau_r QY$ is estimated to be between 60 and 300 ps. This is within the range of prior results on CdSe quantum dots with the same intraband energy[29] We note that the quantum yield is similar for the interband PL of dodecanethiol-capped HgTe CQDs at the same energy,[30] and this suggests that infrared interband and intraband relaxations in CQDs may be both limited by similar relaxation processes. The intraband emission should be explored further as a potential mid-IR light source. In particular, under high excitation, it may exhibit lesser Auger quenching than interband emission due to the very sparse density of state.

The PL in Figure 1E is affected by the doping level and by electron−hole Auger processes since we used an interband excitation at 808 nm. We propose that at $n = 0$ ("1 min" sample after sulfide exposure), intraband PL is quenched due to the rapid ~ps electron hole Auger relaxation from $1P_e$ to $1S_e$, while subsequent recombination with the $1S_e$ electron leads to the interband PL. At $n = 2$ ("4 min" sample before sulfide exposure, and "16 min" sample), it is the interband PL that is quenched by a fast trion Auger decay which moves the hole in $1S_e$, where it can radiatively recombine with a $1P_e$ electron to produce intraband PL. Simultaneous interband and intraband PL is sometimes seen, such as in the 4 min sample after sulfide. It is tentatively attributed to subpopulations with $n = 0$ and $n = 2$ rather than from dual emission by $n = 1$.

Intraband Photodetection. With $n \sim 2$ average doping level, rather long intraband relaxation, and a narrow size distribution, the HgSe CQDs allow for the first test of intraband photoconduction with doped CQDs. For this purpose, films of HgSe CQDs are drop cast on interdigitated electrodes. All the processing is done in air. The films are semitransparent with an optical density of 0.05 to 0.5 at the intraband peak, and thicknesses between 0.1 and 1 μm. The dried films are insulating (>40 MΩ), and the films are cross-linked[1,18,31] by ethanedithiol to render them conductive. Figure 2A shows that the cross-linking does not impact the doping strongly because it is an exchange of thiols. The drop casting and cross-linking are repeated a few times until the film resistance at room temperature is below 100 kΩ.

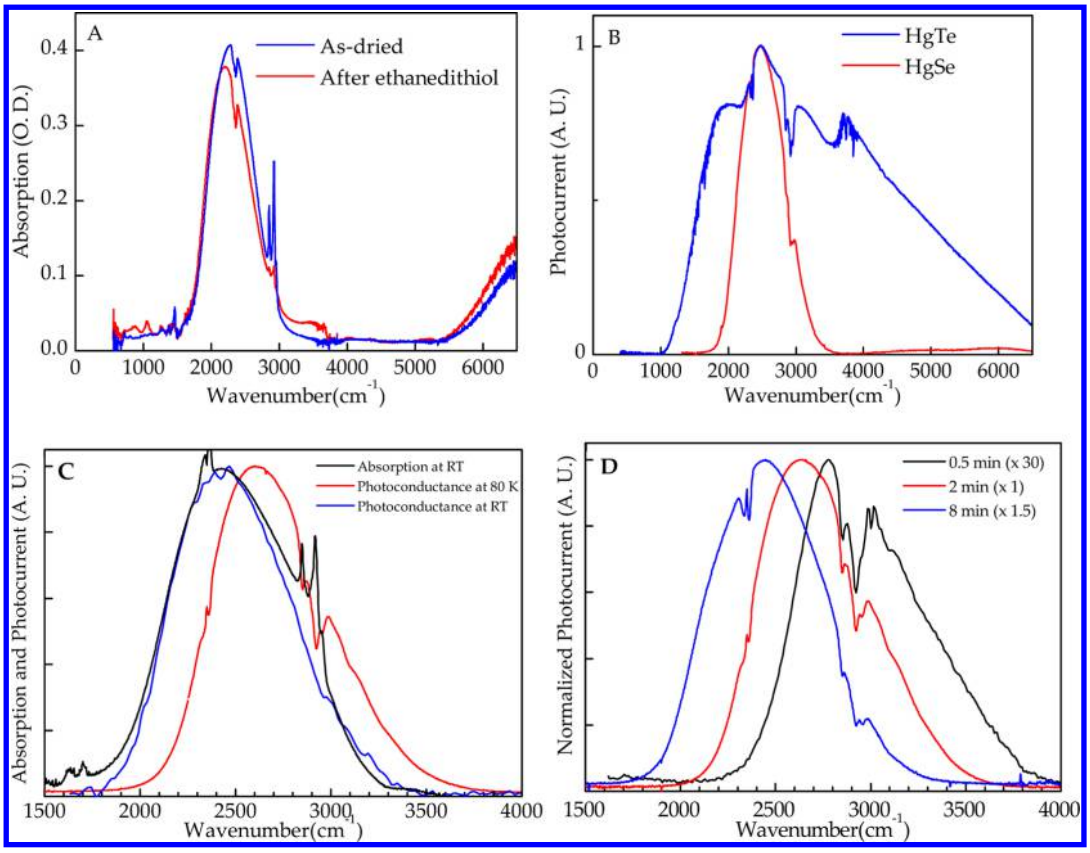

Figure 2. (A) Absorption spectra of dodecanethiol-capped HgSe CQDs on a ZnSe ATR window, deposited from hexane:octane solution and dried (blue line), and after cross-linking with ethanedithiol (red line). The doping is only slightly decreased by this ligand exchange. Sharp features are molecular vibrations from CO_2 (2350 cm^{-1}) and H_2O (3600 cm^{-1}) in the beam path, and from CH stretch (2900 cm^{-1}) and bend modes (1500 cm^{-1}) of the ligands. (B) Photocurrent spectra of an HgSe film (red line) and an HgTe CQD film (blue line), both at 80 K, highlighting the narrow response of the intraband HgSe detector in contrast to the broad response of the interband HgTe. (C) Normalized absorption (black line) and photocurrent (blue line) of a film of HgSe CQD at room temperature. The photocurrent spectrum at 80 K (red line) shows a blue shift of 170 cm^{-1}. (D). Photocurrent with films made with HgSe CQDs at different reaction times, 80 K. Photocurrent spectra are measured with a 10 V bias.

At 80 K, photoconduction spectra are readily obtained. Figure 2B shows a photocurrent spectrum taken in ~1 s, with very good signal-to-noise ratio. Figure 2B also shows that the intraband photoconduction of HgSe CQDs is narrow compared with the interband response of HgTe CQDs. This narrow spectral response of intraband photodection may eliminate the need for spectral filters and facilitate color selectivity of the pixels.

Figure 2C compares the absorption and photocurrent spectra of a HgSe film at room temperature. The absorption is taken with the same CQD sample but with a film made separately on a ZnSe plate, and it shows a perfect match with the intraband photoconduction. Figure 2C also shows a 170 cm^{-1} blue shift of the intraband photoresponse at 80 K. This is typical of all samples and it is interesting as it is opposite to interband HgTe CQDs at similar wavelength, which show red-shifts upon cooling.[19] The gaps of bulk HgSe[32] and HgTe[33] become more negative as the temperature is decreased such that the energy of $1S_e$ decreases, and this partly explains the red shift of HgTe CQDs. However, since the $1P_e$ states also red shifts, it was not clear *a priori* in which direction the $1S_e1P_e$ energy would trend. A two band k.p model predicts essentially no change in the $1S_e1P_e$ energy upon varying the band gap from −0.1 to −0.3 eV and therefore does not explain the blue shift (Supporting Information). Instead, the temperature shift of the energy gap may be assigned to size-dependent electron−phonon effects.[34,35]

Figure 2D shows the photocurrent responses of samples at different reaction times, similar to those shown in Figure 1D. Systematically, the best results are for samples in the middle of the size tuning range because those exhibit the lowest dark current. This is consistent with Figure 1D, where the optimum doping of $n \sim 2$ is obtained with the "4 min" sample. The size also tunes the spectrum which will affect the energy transfer to the hydrocarbon ligands[29] as it approaches the CH stretch (2900 cm^{-1}) or bend vibrations (1500 cm^{-1}) of the remaining organics, but this may be a smaller effect.

Determination of the Mobility in the $1P_e$ State. The mobility of carriers is an important parameter in the discussion of the detector properties. We use electrochemical

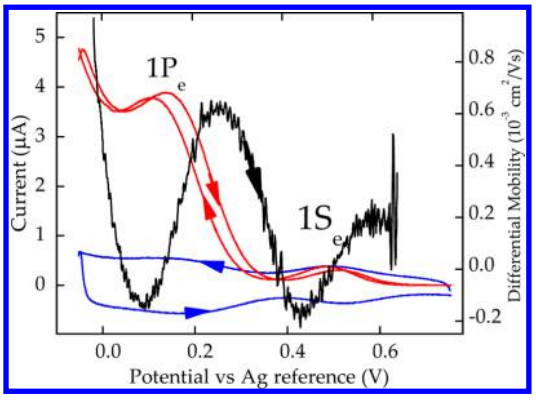

Figure 3. Faradaic current (blue line), conduction current (red line) with 10 mV bias, and differential mobility (black line and right axis) of an HgSe CQD film on a platinum interdigitated electrode. The scanning rate is 80 mV/s and the electrolyte is formamide with tetrabutylammonium perchlorate (0.1 M). The reversible reduction/oxidation peaks around 0.5 and 0.15 V correspond to electron injection into the $1S_e$ state and the $1P_e$ state, respectively. The conduction minimum at ~0.35 V occurs when the $1S_e$ state is filled. A second minimum at ~0 V is a conductivity gap between $1P_e$ and higher states. The arrows indicate the scanning direction.

gating since it can inject many more charges than solid state gating[1] and can separately give the mobility in the $1S_e$ and $1P_e$ states.[31] Figure 3 shows the cyclic voltammetry of a film of HgSe CQDs measured with a bipotentiostat. The sequential charging/discharging of the $1S_e$ and $1P_e$ levels appear as reversible peaks in the faradaic (charge injection) current. The conductivity gap between $1S_e$ and $1P_e$ is also clearly evidenced by the dip in the conduction current. A second conductivity gap is seen above $1P_e$ in Figure 3 which indicates that the state separation in the HgSe CQDs is very well-defined. The differential mobility gives a higher mobility for $1P_e$ compared to $1S_e$. This was reported for CdSe previously[31] and attributed to a larger density of state and smaller potential barrier. The differential mobility indicates a value of 6.0×10^{-4} cm^2/(V s) for the $1P_e$ state. Using the Einstein's relation between mobility and diffusion, a hopping time[31] τ_h ~5 ns is estimated.

Detector Properties. We measured the detecting properties of many films of CQDs in the middle of the size range. With thin films that are partially absorbing (10−20% at the peak) and with a 10 V bias, the responsivity is typically around 5×10^{-4} A/W, flat between 50 and 600 Hz chopping frequency and changing by less than a factor of 2 between 300 and 80 K. Increasing the bias increases the responsivity but increases the dark current even more (Supporting Information). At 94 V bias, the maximum responsivity obtained so far is $\sim 5 \times 10^{-3}$A/W and starts to saturate. By including corrections for the ZnSe window transmission 70%, and the masking by the electrodes, 60%, the maximum responsivity would be $\sim 1.2 \times 10^{-2}$A/W.

The responsivity of a detector is given by R = (current)/(input power)) = $eg\eta/h\nu$ where e is the electron charge, g is the gain, η is defined as the quantum efficiency, h is Planck constant and ν is the light frequency. Assuming unity gain and quantum efficiency, the responsivity at 5 μm should be 2.5 A/W. The typical result of 5×10^{-4} A/W at 10 V bias gives η of 2×10^{-4}, while the responsivity at the highest bias is only about 0.5% of the ideal responsivity. Part of the reason must be the limited charge separation efficiency associated with the short $1P_e$ lifetime compared to the hopping time. An estimate of the charge separation efficiency is $\eta \sim \tau_h/(\tau_1 + \tau_h) \sim 2-10\%$. This is higher than measured and suggests that faster recombination centers are present, possibly as defective nanocrystals. Higher responsivity can be obtained by adding gain, but this will not increase the detectivity. Instead it will be necessary to investigate alternative cross-linking materials and ligands to increase the $1P_e$ state lifetime and reduce the hopping time.

The detectivity is more sample dependent due to variations in the dark current. The best detectivity at 80 K was measured on a sample with a ~ 2250 cm^{-1} detection peak at 80 K for which the dark current decreased by a factor of 3200 from 300 K to 80 K. At 80 K and 500 Hz, the measured current noise spectral density i_n = 44 fAHz$^{-1/2}$ and close to shot noise limited, while the responsivity was 0.38 mA/W. Using $D^* = A^{1/2}R/i_n$, where i_n is the current noise spectral density and A is the sample area of 1 mm^2, $D^* = 8.5 \times 10^8$ Jones at 500 Hz. Correcting for the masking by the electrode where only 60% of the area is active, and the transmission of the uncoated ZnSe window of 70%, leads to a $D^* = 2 \times 10^9$ Jones with a partially absorbing film (10−20%). Commercial InSb bulk detectors operating at the same wavelength and temperature have $D^* \sim 10^{11}$ Jones.

In the shot noise limit of the generation recombination current, the specific detectivity for photoconduction can be written as

$$D^* = \frac{\eta}{h\upsilon\sqrt{\frac{2n_{th}t}{\tau}}} \quad (1)$$

where n_{th} is the thermal carrier density, t is the sample thickness, and τ is the carrier lifetime.[14] It is assumed that the measurement frequency is high enough so that $1/f$ noise can be neglected. When the noise from the background thermal photon flux Φ dominates, the detector is in the background limited infrared photodetection (BLIP) condition. The BLIP limit is $D^* = (\eta/h\nu)(\Phi)^{1/2}$.[14] At 77 K, commercial InSb and HgCdTe (MCT) detectors operate close to the BLIP limit, therefore research is aimed at making cheaper detectors, operating at higher temperature, suitable for microfabrication and with higher uniformity from pixel to pixel. Above 77 K, the detectivity of InSb and MCT detectors drops because of the increase of the thermal carrier density and also because the carrier lifetime shortens due to the onset of Auger processes.[36]

Using eq 1, we evaluate the expected D^* for our samples. For the carrier density, we use $n_{th} = (n'_{th}/V_{NC})$

where n_{th}' is the number of thermal carrier per nanocrystal and V_{NC} is the volume occupied per nanocrystals. At the ideal doping of $n = 2$, $n_{th}' = (N_{1S}N_{1P})^{1/2}\exp(-h\nu/2kT)$, where $N_{1S} = 2$, $N_{1P} = 6$ are the level degeneracy. Assuming purely geminate recombination, the carrier lifetime is $\tau = (\tau_1/n_{th}')$, eq 1 becomes $D^* = \eta((\tau_1 V_{NC})/(2t))^{1/2}/h\nu n_{th}'$. We use a 5 μm detection wavelength, $\eta = 2 \times 10^{-4}$, a thickness of 100 nm, $\tau_1 = 100$ ps and $V_{NC} = 1.4 \times 10^{-18}$ cm^3. At 300 K, $n_{th}' = 2.5 \times 10^{-2}$ and $D^* = 7.6 \times 10^6$ Jones. This is in line with the lower signal level at room temperature but we note that, at 300 K, the measured detectivity is lower due to the fact that the noise is already dominated by 1/f noise at 500 Hz. At 80 K, the calculated carrier concentration per dot drops to 2.9×10^{-8} and D^* should correspondingly increase to 6.3×10^{11} Jones. This is 300 times better than the best measured value and above the BLIP limit. Part of the discrepancy is that the largest measured drop in the dark current was ~3000 instead of the expected 6 orders of magnitude, and this can be attributed to a deviation from the $n = 2$ doping. Thus, larger D^* should be possible even with the present materials.

Performance Perspective. Epitaxial quantum dots photodetectors have been much investigated previously.[37−39] While their performances have improved significantly over the past decade,[40−43] they still struggle to match the bulk MCT performances.[44] The first intraband detector demonstrated here with doped CQDs shows already very promising spectral response and operation at room temperature.

It is therefore instructive to evaluate the optimum performance achievable with CQDs detectors as done previously for epitaxial quantum dots.[14] In principle, intraband CQDs will allow higher operating temperature because they can circumvent the Auger processes with their sparse density of states.[14] Although the lifetime is presently limited by nonradiative processes giving rise to the low PL quantum yield discussed earlier, we can expect that future improvements will raise the lifetime. Choosing a detector thickness equal to the absorption length, Einstein's relation between absorption and radiative lifetime gives $(\tau_r/t) = (\lambda^2)/(8\pi V_{NC}\Delta\nu)$, where λ is the wavelength of light and $\Delta\nu$ is the resonance width (Supporting Information). In the radiative lifetime limit and in the intrinsic regime, the carrier lifetime is $\tau = \tau_r/n_{th}'$. The maximum detectivity becomes

$$D^*_{max} = \frac{c}{4h\nu^{5/2}n_{th}'\sqrt{\pi^{\Delta\nu/\nu}}} \quad (2)$$

where c is the speed of light. The material dependence is only in the thermal carrier density per quantum dot, indicating that undoped interband and doped intraband ($n = 2$) CQDs will have similar D^*_{max}. There may be practical differences in whether it is possible to approach the radiative limit, but the similar PLQY of HgTe interband and HgSe intraband CQDs for the same wavelengths do not yet indicate that this will the case.

Using $\eta = 1$ and a bandwidth $(\Delta\nu/\nu) = 20\%$, the maximum detectivity of a 5 μm intraband CQD detector is then $D^*_{max} = 2.1 \times 10^{10}$ Jones at 300 K, which is about an order of magnitude better than microbolometers. CQDs have therefore the potential to be useful for room temperature detection while also allowing fast imaging, cheap fabrication and color specificity, and this justifies further investigations of the CQD infrared detectors. The BLIP limit would be reached at ~215 K allowing also to reduce the cooling requirements compared to existing semiconductor technology. With nonradiative processes and a nonunity quantum yield of charge separation, the detectivity becomes $D^* = \eta(QY)^{1/2}D^*_{max}$. To increase the detectivity, the strategy will be to increase the photoluminescence quantum yield and the charge separation efficiency while maintaining the control on the doping level.

The β-HgS CQDs also show doping in ambient conditions,[24] and intraband photoconduction was observed as well but it exhibits a lower signal-to-noise level (Supporting Information). HgSe and HgS CQDs are the only ones known to have stable doping in ambient at the moment and they are zero gap or narrow gap, respectively. A broader application of the intraband transitions will require doping carriers in wider bang gap materials, a challenge that may be solved for some systems and in the proper chemical environment using impurity doping[11−13] or charge transfer doping.[45]

CONCLUSION

In summary, this is the first report of photoconduction based on the intraband transitions of doped colloidal quantum dots. The materials also exhibit intraband photoluminescence, which may lead to an alternative approach to mid-IR light sources. This advance results from prior progress in the understanding of intraband relaxation, conductivity and doping of colloidal quantum dots, and opens new perspectives for colloidal quantum dots. In contrast to interband transitions of quantum dots, the intraband transition provides a selective spectral detection and it should broaden the range of materials in the search for high performance and affordable infrared detection.

METHODS

HgSe CQD Synthesis. 12.6 mg of selenourea (0.1 mmol, Aldrich, 98%) was dissolved in 1 mL of oleylamine (Aldrich, 70%) by heating at 180 °C for 2 h under nitrogen in the glovebox, yielding a clear, light brown solution. In the meantime, 27.2 mg of mercury(II) chloride, $HgCl_2$ (0.1 mmol, Aldrich, 99.999%,) was

added to 4 mL of oleylamine, and the mixture was heated at 110 °C for about 30 min to dissolve the $HgCl_2$ crystal, forming a clear solution. Then the selenourea/oleylamine solution was injected quickly into the mixture, and the mixture turned black immediately. The particles were quite stable in the reaction, even after growing 12 h. The final particle size could be controlled by varying the reaction time. To stop the reaction, 8 mL of a "quench solution", which was made of 5% TOP, 10% dodecanethiol and 85% TCE, was added to the reaction mixture. The quenched mixture was precipitated with methanol, centrifuged, and the precipitate was redispersed in TCE. The product TCE solution was stable and could be stored for months without aggregation. TEM images of the three extracts are shown in Figures S1, S2, and S3.

Sulfide Deposition Using c-ALD. 1 mL of formamide, 50 μL of oleylamine and 150 μL of 0.1 M $(NH_4)_2S$ were added to 1 mL of HgSe CQD solution in tetrachloroethylene. This mixture was stirred for about 5 min, and then the HgSe dots were washed twice with formamide to remove excess $(NH_4)_2S$. Then the HgSe CQD solution was ready for the FTIR and other measurements.

Ligand Exchange in QD Films. The dried films are dipped for 10 s in a solution of ethanol and 2% ethanedithiol and 2% HCl and then rinsed with ethanol.

Photoluminescence Measurement. The cleaned HgSe CQD solution in TCE are transferred into a liquid cell and photoexcited by 808 nm continuous laser chopped at 70 kHz. The photoluminescence is measured with a step-scan FTIR with an MCT detector and a lock-in amplifier. The reported spectra are not corrected for the spectrometer and detector response. Quantum yields are measured with an integrating sphere following ref 21 of the main text.

Absorption of Films. The colloidal samples are cleaned by precipitation and dispersed in hexane:octane (9:1), and then they are drop cast on a ZnSe ATR plate.

Photoconductance. Photoconductance spectra are measured with a standard Nicolet 550 FTIR. The internal light is sent through the external port and focused on the sample with a 5 cm effective focal length parabolic gold mirror. The samples are biased with a 9 V battery in series with a matched resistance. The voltage across the sample is sent to a SR560 AC voltage amplifier with a gain of 200 before being sent back to the FTIR input.

The responsivity is measured using a calibrated blackbody source, Omega BB4A, at 873 K. A chopper modulates the light up to 600 Hz. The sample is inside a cryostat behind a ZnSe uncoated window and ~140 mm from the source. A bias of 10 V is applied and the current is amplified with a Femto DLPCA-200 before the SR560AC voltage amplifier. The power on the sample is calculated by integrating from 2200 to 2700 cm^{-1} the blackbody spectrum at 873 K, using the known size of 21 mm diameter of the source and the approximate distance to the sample. This should be accurate within a factor of 2.

For the detectivity, we used the responsivity determined above. For the current noise spectral density measurements, the sample is biased at 10 V with the DC amplifier Femto DLPCA-200. The gain is adjusted so that the output is below the maximum output of the DLPCA-200 of 10 V. The voltage is then amplified by the SR560AC voltage amplifier at gains between 1 and 100. The voltage noise spectral density $V/Hz^{1/2}$ is obtained directly with a spectrum analyzer, SR760 and its value at 500 Hz is recorded. The sample current noise spectral density is obtained from the voltage noise spectral density by dividing by the total gain.

Figure S4 shows the responsivity and dark current of a film of HgSe CQDs as a function of bias at 80 K. The responsivity starts to saturate around 90 V but the dark current increases nonlinearly.

Figure S5 shows a photoconductance spectrum obtained with HgS nanocrsytals.

Electrochemistry. For the spectroelectrochemical data shown in Figure S6, a hexanedithiol cross-linked HgSe CQD film was dried on a platinum disk for 30 min under vacuum and placed into an electrochemical cell. The spectroelectrochemical cell is comprised of three electrodes: an Ag pseudo reference electrode, the Pt working electrode and an Pt counter electrode. Tetrabutylammonium perchlorate (TBAP, 0.1 M) in anhydrous acetonitrile was injected into the electrochemical cell inside the glovebox. The electrochemical cell was placed inside of the FTIR, the Pt electrode was lightly pressed against a CaF_2 window and the infrared light reflected from the Pt working electrode was collected by an MCT detector.

Figure S6 shows the difference absorption spectra, with the absorption spectrum at +1 V (most oxidizing potential), at varying applied biases up to −2.2 V (most reducing). In the reducing direction, the interband absorption is increasingly bleached while the intraband absorption rises, confirming that the HgSe is doped n-type.

For the cyclic voltammetry and conductance data shown in Figure 3 of the main text, CQD film were deposited on an interdigitated electrode (CH Instruments, Inc., 10 μm width, 5 μm interval, 2 mm length) and cross-linked with ethanedithiol as described above. The samples were immersed in a 0.1 M tetrabutylammonium perchlorate (TBAP) in formamide. A silver wire pseudoreference and a Pt counter electrode were used. The measurements are done in air. The hopping time is obtained using $\mu = ed^2/6\tau_h kT$ where d is the center to center particle distance taken to be 7 nm.

The differential mobility is obtained by taking the faradaic current, subtracting a constant capacitive component to extract the current of charges injected in the dots. This is then integrated to get the charge injected in the CQDs Q (V). The conduction current is used to get the conductance G (V). Both are proportional to the number of digits, the length and the thickness of the film but the charge is proportional to the full width of the electrodes and gap, while the conductance is inversely proportional to the gap only. The differential mobility μ is numerically obtained as $\mu = dG/dQ \times w(w_0 + w)$ where w is the gap between the electrodes and w_0 is the width of the electrodes. The differential mobility discussed in the main text is numerically obtained as dG/dQ.

Conflict of Interest: The authors declare no competing financial interest.

Acknowledgment. This work was supported by the US National Science Foundation (NSF; Grant DMR-1104755). The authors made use of shared facilities supported by the NSF MRSEC Program under DMR-0820054.

Supporting Information Available: Theoretical calculations of the optimal detectivity and k.p model, TEMs of different-sized HgSe CQDs, responsivity and dark current data for a HgSe CQD film under higher bias, absorption and photocurrent of a HgS CQD film, difference absorption spectra of a HgSe CQD film under electrochemical potential, two-band k.p results for the $1S_e-1P_e$ transition energy and the oscillator strength. This material is available free of charge *via* the Internet at http://pubs.acs.org.

REFERENCES AND NOTES

1. Talapin, D. V.; Lee, J.-S.; Kovalenko, M. V.; Shevchenko, E. V. Prospects of Colloidal Nanocrystals for Electronic and Optoelectronic Applications. *Chem. Rev.* **2010**, *110*, 389–445.
2. Faist, J. *Quantum Cascade Lasers*; Oxford University Press: Oxford, U.K., 2013.
3. West, L. C.; Eglash, S. J. First Observation of an Extremely Large-Dipole Infrared Transition within the Conduction-Band of a Gaas Quantum Well. *Appl. Phys. Lett.* **1985**, *46*, 1156–1158.
4. Levine, B. F.; Choi, K. K.; Bethea, C. G.; Walker, J.; Malik, R. J. New 10 μm Infrared Detector Using Intersubband Absorption in Resonant Tunneling GaAlAs Superlattices. *Appl. Phys. Lett.* **1987**, *50*, 1092–1094.
5. Faist, J.; Capasso, F.; Sivco, D. L.; Sirtori, C.; Hutchinson, A. L.; Cho, A. Y. Quantum Cascade Laser. *Science* **1994**, *264*, 553–556.
6. Klimov, V. I.; McBranch, D. W. Femtosecond 1P-to-1S Electron Relaxation in Strongly Confined Semiconductor Nanocrystals. *Phys. Rev. Lett.* **1998**, *80*, 4028–4031.
7. Kambhampati, P. Hot Exciton Relaxation Dynamics in Semiconductor Quantum dots: Radiationless Transitions on the Nanoscale. *J. Phys. Chem. C* **2011**, *115*, 22089–22109.

8. Sambur, J. B.; Novet, T.; Parkinson, B. A. Multiple Exciton Collection in a Sensitized Photovoltaic System. *Science* **2010**, *330*, 63–66.
9. Semonin, O. E.; Luther, J. M.; Choi, S.; Chen, H.-Y.; Gao, J.; Nozik, A. J.; Beard, M. C. Peak External Photocurrent Quantum Efficiency Exceeding 100% *via* MEG in a Quantum Dot Solar Cell. *Science* **2011**, *334*, 1530–1533.
10. Peterson, M. D.; Cass, L. C.; Harris, R. D.; Edme, K.; Sung, K.; Weiss, E. A. The Role of Ligands in Determining the Exciton Relaxation Dynamics in Semiconductor Quantum Dots. *Annu. Rev. Phys. Chem.* **2014**, *65*, 317–339.
11. Norris, D. J.; Efros, A. L.; Erwin, S. C. Doped Nanocrystals. *Science* **2008**, *319*, 1776–1779.
12. Mocatta, D.; Cohen, G.; Schattner, J.; Millo; Rabani, E.; Banin, U. Heavily Doped Semiconductor Nanocrystal Quantum Dots. *Science* **2011**, *332*, 77–81.
13. Sahu, A.; Kang, M. S.; Kompch, A.; Notthoff, C.; Wills, A. W.; Deng, D.; Winterer, M.; Frisbie, C. D.; Norris, D. J. Electronic Impurity Doping in CdSe Nanocrystals. *Nano Lett.* **2012**, *12*, 2587–2594.
14. Phillips, J. Evaluation of the Fundamental Properties of Quantum Dot Infrared Detectors. *J. Appl. Phys.* **2002**, *91*, 4590–4594.
15. Bhattacharya, P.; Ghosh, S.; Stiff-Roberts, A. D. Quantum Dot Opto-Electronic Devices. *Annu. Rev. Mater. Res.* **2004**, *34*, 1–40.
16. Benisty, H.; Sotomayor-Torrès, C. M.; Weisbuch, C. Intrinsic Mechanism for the Poor Luminescence Properties of Quantum-Box Systems. *Phys. Rev. B: Condens. Matter Mater. Phys.* **1991**, *44*, 10945–10948.
17. Rauch, T.; Böberl, M.; Tedde, S. F.; Fürst, J.; Kovalenko, M. V.; Hesser, G.; Lemmer, U.; Heiss, W.; Hayden, O. Near-Infrared Imaging with Quantum-Dot-Sensitized Organic Photodiodes. *Nat. Photonics* **2009**, *3*, 332–336.
18. Konstantatos, G.; Sargent, E. H. Colloidal Quantum Dot Photodetectors. *Infrared Phys. Technol.* **2011**, *54*, 278–282.
19. Keuleyan, S.; Lhuillier, E.; Brajuskovic, V.; Guyot-Sionnest, P. Mid-Infrared HgTe Colloidal Quantum Dot Photodetectors. *Nat. Photonics* **2011**, *5*, 489–493.
20. Stiff-Roberts, A. D.; Lantz, K. R.; Pate, R. Room-Temperature, Mid-Infrared Photodetection in Colloidal Quantum Dot/Conjugated Polymer Hybrid Nanocomposites: A New Approach to Quantum Dot Infrared Photodetectors. *J. Phys. D: Appl. Phys.* **2009**, *42*, 234004.
21. Kershaw, S. V.; Susha, A. S.; Rogach, A. L. Narrow Bandgap Colloidal Metal Chalcogenide Quantum Dots: Synthetic Methods, Heterostrcutres, Assemblies, Electronic and Infrared Optical Properties. *Chem. Soc. Rev.* **2013**, *42*, 3033–3087.
22. Kuno, M.; Higginson, K. A.; Qadri, S. B.; Yousuf, M.; Lee, S. H.; Davis, B. L.; Mattoussi, H. Molecular Clusters of Binary and Ternary Mercury Chalcogenides: Colloidal Synthesis, Characterization, and Optical Spectra. *J. Phys. Chem. B* **2003**, *107*, 5758–5767.
23. Oh, S. J.; Berry, N. E.; Choi, J. H.; Gaulding, E. A.; Paik, T.; Hong, S. H.; Murray, C. B.; Kagan, C. R. Stoichiometric Control of Lead Chalcogenide Nanocrystal Solids to Enhance Their Electronic and Optoelectronic Device Performance. *ACS Nano* **2013**, *3*, 2413–2421.
24. Jeong, K. S.; Deng, Z.; Keuleyan, S.; Liu, H.; Guyot-Sionnest, P. Air-Stable N-Doped Colloidal HgS Quantum Dots. *J. Phys. Chem. Lett.* **2014**, *5*, 1139–1143.
25. Brown, P. R.; Kim, D.; Lunt, R. R.; Zhao, N.; Bawendi, M. G.; Grossman, J. C.; Bulovic, V. Energy Level Modification in Lead Sulfide Quantum Dot Thin Films through Ligand Exchange. *ACS Nano* **2014**, *8*, 5863–5872.
26. Ithurria, S.; Talapin, D. V. Colloidal Atomic Layer Deposition (c-ALD) Using Self-Limiting Reactions at Nanocrystal Surface Coupled to Phase Transfer Between Polar and Nonpolar Media. *J. Am. Chem. Soc.* **2012**, *134*, 18585–18590.
27. Guyot-Sionnest, P.; Shim, M.; Matranga, C.; Hines, M. A. Intraband Relaxation in CdSe Quantum Dots. *Phys. Rev. B: Condens. Matter Mater. Phys.* **1999**, *60*, R2181–R2184.
28. Efros, A. L.; Kharchenko, V. A.; Rosen, M. Breaking the Phonon Bottleneck in Nanometer Quantum Dots: Role of Auger-Like Processes. *Solid State Commun.* **1995**, *93*, 281–284.
29. Pandey, A.; Guyot-Sionnest, P. Slow Electron Cooling in Colloidal Quantum Dots. *Science* **2008**, *322*, 929–932.
30. Keuleyan, S.; Kohler, J.; Guyot-Sionnest, P. Photoluminescence of Mid-Infrared Hgte Colloidal Quantum Dots. *J. Phys. Chem. C* **2014**, *118*, 2749–2753.
31. Yu, D.; Wang, C. J.; Guyot-Sionnest, P. N-Type Conducting Cdse Nanocrystal Solids. *Science* **2003**, *300*, 1277–1280.
32. Dobrowolska, M.; Dobrowolski, W.; Mycielski, A. Temperature Study of Interband $\Gamma 6 \rightarrow \Gamma 8$ Magnetoabsorption in HgSe. *Solid State Commun.* **1980**, *34*, 441–445.
33. Man, P.; Pan, D. S. Infrared Absorption in HgTe. *Phys. Rev. B: Condens. Matter Mater. Phys.* **1991**, *44*, 8745–8758.
34. Olkhovets, A.; Hsu, R.-C.; Lipovskii, A.; Wise, F. W. Size-Dependent Temperature Variation of the Energy Gap in Lead-Salt Quantum Dots. *Phys. Rev. Lett.* **1998**, *81*, 3539–3542.
35. Dey, P.; Paul, J.; Bylsmaa, J.; Karaiskaj, D.; Luther, J. M.; Beard, M. C.; Romero, A. H. Origin of the Temperature Dependence of the Band Gap of Pbs and Pbse Quantum Dots. *Solid State Commun.* **2013**, *165*, 49–54.
36. Chang, Y.; Grein, C. H.; Zhao, J.; Sivananthan, S.; Flatte, M. E.; Liao, P. K.; Aqariden, F. Carrier Recombination Lifetime Characterization of MBE-Grown HgCdTe. *Appl. Phys. Lett.* **2008**, *93*, 192111.
37. Berryman, K. W.; Lyon, S. A.; Segev, M. Mid-Infrared Photoconductivity in InAs Quantum Dots. *Appl. Phys. Lett.* **1997**, *70*, 1861–1863.
38. Pan, D.; Towe, E.; Kennerly, S. Normal-Incidence Intersubband (In, Ga)As/GaAs Quantum Dot Infrared Photodetectors. *Appl. Phys. Lett.* **1998**, *73*, 1937–1939.
39. Sauvage, S.; Boucaud, P.; Brunhes, T.; Immer, V.; Finkman, E.; Gerard, J. M. Midinfrared Absorption and Photocurrent Spectroscopy of InAs/GaAs Self-Assembled Quantum Dots. *Appl. Phys. Lett.* **2001**, *78*, 2327–2329.
40. Stiff, A. D.; Krishna, S.; Bhattacharya, P.; Kennerly, S. W. Normal-Incidence, High-Temperature, Mid-Infrared, InAs-GaAs Vertical Quantum-Dot Infrared Photodetector. *IEEE J. Quantum Electron.* **2001**, *37*, 1412–1419.
41. Chakrabarti, S.; Stiff-Roberts, A. D.; Su, X. H.; Bhattacharya, P.; Ariyawansa, G.; Perera, A. G. U. High-Performance Mid-Infrared Quantum Dot Infrared Photodetectors. *J. Phys. D: Appl. Phys.* **2005**, *38*, 2135–2141.
42. Lim, H.; Tsao, S.; Zhang, W.; Razeghi, M. High-Performance Quantum-Dot Infrared Photodetectors Grown on InP Substrate Operating at Room Temperature. *Appl. Phys. Lett.* **2007**, *90*, 131112.
43. Wu, J.; Shao, D. L.; Dorogan, V. G.; Li, A. Z.; Li, S. B.; DeCuir, E. A.; Manasreh, M. O.; Wang, Z. M.; Mazur, Y. I.; Salamo, G. J. Intersublevel Infrared Photodetector with Strain-Free GaAs Quantum Dot Pairs Grown by High-Temperature Droplet Epitaxy. *Nano Lett.* **2010**, *10*, 1512–1516.
44. Martyniuk, P.; Rogalski, A. Quantum-Dot Infrared Photodetectors: Status and Outlook. *Prog. Quantum Electron.* **2008**, *32*, 89–120.
45. Shim, M. Guyot-Sionnest, P. N-Type Colloidal Semiconductor Nanocrystals. *Nature* **2000**, *407*, 981–983.